



Bubble convection and bubbly flow turbulent time and length scales in two-dimensional plunging jets

Rui Shi, Hang Wang*, Hubert Chanson

The University of Queensland, School of Civil Engineering, Brisbane, QLD 4072, Australia

ARTICLE INFO

Keywords:

Plunging jet
Air entrainment
Bubble clustering
Integral turbulent scales
Schmidt number

ABSTRACT

Air entrainment and air-water mixing by a flow impingement are enhanced by the turbulent shear layer and associated instabilities in the receiving waterbody. This paper presents an experimental study aiming at a quantitative description of bubble-turbulence interplay in two-dimensional supported plunging water jets. In addition to the basic air-water flow properties, the turbulence intensity in the highly-aerated plunging pool was estimated based on void fraction and total pressure fluctuation measurements, while the turbulent time and length scales were recorded systematically. The coupling of bubble convection and formation of macroscopic turbulent structures was characterised in terms of bubble clustering behaviours and turbulent length and time scales of the bubbly flow eddy structures. The effects of jet impact velocity were investigated for a fixed jet length. These advanced data analyses were applied to plunging jet two-phase flow for the first time. The results would provide new benchmark data for numerical modelling of intense air-water flow at a higher level than the basic two-phase flow dynamic properties. A discussion was developed at the end on the turbulent length scales and the Schmidt number in the bubbly flow regions of horizontal hydraulic jump and vertical supported plunging jet.

1. Introduction

Air-water two-phase flow is a major concern in the study and application of mass and heat transfer because it induces substantial change in interfacial area [1,2]. Self-sustained air entrainment into water may be achieved by inducing free-surface breaking. A canonical case is a plunging jet, where air is entrained at the intersection between the impinging jet and receiving bath [3,4]. The impingement point is a discontinuity in free-surface profile, velocity and pressure fields. In addition to the source of aeration, it also acts as the origin of a turbulent shear layer between the high-speed jet core and the ambient water in the receiving pool [5]. The development of turbulent instabilities enhances the air entrainment and bubble convection, and large entrained air bubbles are broken into small ones by the turbulent shear forces, enlarging significantly the air-water interfacial area. The mass and heat transfer is also enhanced by the increase in submerged bubble lifetime associated with the longer advection distance and recirculating motion. The presence of air bubbles further modifies the turbulence field by bubble deformation, thus influencing the energy dissipation. A prerequisite for the understanding of all these physical processes is a quantitative description and interpretation of the bubble-turbulence interplay.

To date, the most reliable method to investigate air-water open channel flow at high Reynolds numbers is still physical modelling, and successful measurement techniques include flow imaging and intrusive phase detection [6,7]. Although numerical simulation has the potential to provide detailed flow characterisation, the model must be verified at a proper level [8,9]. For example, a numerical prediction of eddy lifetime cannot only be verified using the time-averaged void fraction or velocity distributions, but also has to involve experimentally-quantified turbulent time scale data [10,11]. A recent numerical study of hydraulic jump by Mortazavi et al. [12] presented for the first time the model verification using the integral turbulent length scale. For plunging jet flows, most literature on air-water flow measurement focused on basic two-phase flow properties such as void fraction, air- or water-phase velocity, air entrainment rate, bubble size, penetration depth, etc., with few attempts at turbulence measurement [13–18]. There is basically no benchmark data that quantify the bubble-turbulence interaction in detail.

The present study presented an attempt to measure the bubbly flow structures in highly-aerated plunging jets. The quantitative parameters adopted to describe the coupling between bubble convection and flow turbulence included the bubble clustering properties and characteristic turbulent length and time scales, which were applied to plunging jets

* Corresponding author.

E-mail address: hang.wang@uqconnect.edu.au (H. Wang).

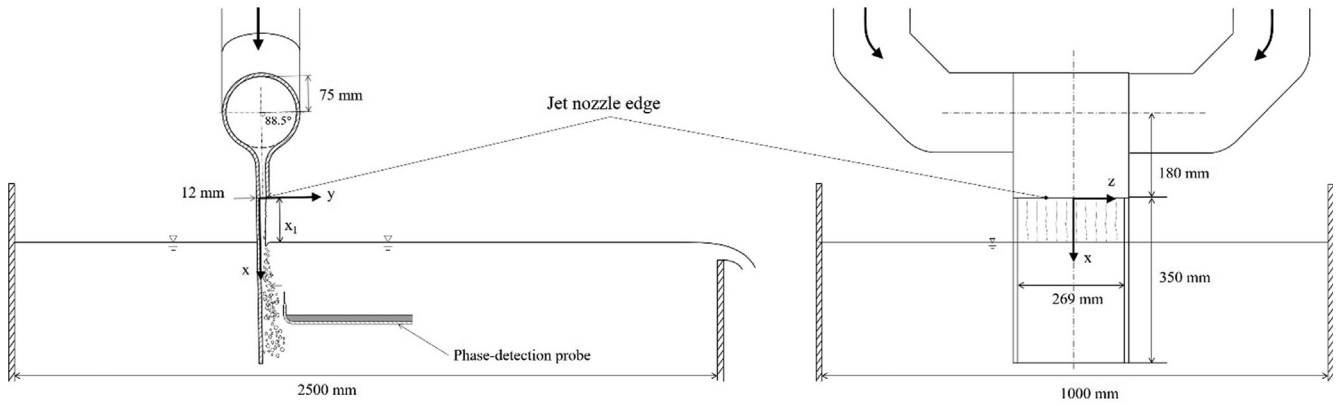


Fig. 1. Definition sketch of planar plunging jet experimental setup: side view (left) and front view (right).

for the first time. The measurements were conducted using a series of intrusive conductivity phase-detection probes. The key results are presented after basic characterisation of the air-water flow, followed by a comparative discussion on the turbulent length scale data in horizontal hydraulic jump and vertical supported plunging jet.

2. Experimental facility and instrumentation

The experimental facility consisted of a rectangular jet nozzle and a receiving water tank. The jet nozzle was 0.269 m wide, with a 0.012 m opening that equalled to the initial jet thickness d_0 . A quasi-two-dimensional planar water jet was discharged downwards into a 2.5 m long, 1 m wide, 1.5 m deep receiving bath. The planar jet was supported on one side by a full-width PVC sheet extending 0.35 m from the nozzle edge. The jet support was built with transparent sidewalls that constrained the falling jet within the width of the support and enabled flow visualisation. The jet nozzle and support system was set to 88.5° from the horizontal to prevent jet detachment. The large-size receiving water tank ensured the air-water flow in the plunging pool free of boundary effects. A sharp-crested weir at the far end of the tank allowed for a constant water level control during the experiments. Fig. 1 shows a sketch of the experimental system, where the longitudinal coordinate x originated from the nozzle edge and the normal coordinate y (perpendicular to the jet support) from the jet support plane.

The water discharge was measured with an orifice or Venturi meter that was calibrated onsite, with expected percentage of error within $\pm 2\%$. A mass conservation check based on velocity and void fraction measurements in the falling jet confirmed adequate accuracy of the flow rate measurement. Two fine-adjustment travelling mechanisms were used to control the translation of flow-measuring probes in the longitudinal and normal directions. The probe position was read from two linear position sensors that provided accuracy within 0.05 mm.

The air-water flow properties were measured using a series of dual-tip phase-detection probes. Each probe had two phase-detection needle sensors that were mounted parallel to each other and both against the flow direction, with a difference Δx in sensor length. Each needle sensor detected air-water interfaces on the sensor tip based on the change in electrical conductivity of air and water phases between the central electrode ($\varnothing = 0.25$ mm) and the outer electrode ($\varnothing = 0.80$ mm) of the sensor. Both sensors were sampled simultaneously at 20 kHz for 90 s at each measurement location. A total of six dual-tip phase-detection probes with different $\Delta x = 2.4$ mm, 4.9 mm, 7.1 mm, 9.9 mm, 16.0 mm and 25.0 mm were used to enable measurements of integral turbulent length and time scales (see Section 3.4).

For a number of experiments, a total pressure probe was mounted side by side to the phase-detection probe to quantify the turbulence intensity in the bubbly flow (see Section 3.2). The pressure sensor had a 5 mm external diameter with a 1 mm diameter silicon diaphragm

detecting the instantaneous stagnation pressure. The absolute pressure measurement range was 0–1.5 bars. The centre of the pressure sensor head was at the same longitudinal and normal positions as the phase-detection probe leading tip, with a transverse separation of 6.2 mm. The total pressure sensor was sampled simultaneously with the phase-detection probe at 20 kHz.

3. Data processing

3.1. Basic air-water flow properties

The individual bubble detection was analysed using the binarised phase-detection signal, where a 50% threshold between the maximum possibilities of air and water phases was adopted. Voltage samples above the threshold were converted to an instantaneous void fraction of 0 in water, and those below the threshold were converted to a void fraction of 1 in air. The binarised signal provided the local time-averaged void fraction and bubble count rate within the sampling duration. The results presented in this paper are the ensemble-averaged values of six phase-detection probes.

3.2. Velocity and turbulence intensity

The velocity of air-water interfaces in high-speed bubbly flow was found to be very close to the flow velocity, and the non-slip condition held [19,20]. The interfacial velocity was measured between the two phase-detection sensor tips aligned in the longitudinal direction. A cross-correlation between the sensor signals showed a maximum correlation coefficient $R_{xy,max}$ at a time lag T , and the longitudinal interfacial velocity equalled to

$$V = \frac{\Delta x}{T} \quad (1)$$

Δx being the longitudinal separation distance between the sensor tips. The longitudinal velocity component is deemed to be equal to the interfacial velocity in the jet core region.

The velocity fluctuations were derived from total pressure measurement in the bubbly flow, assuming a negligible static pressure fluctuation. The density variation associated with the discontinuous two-phase flow was approximated using the local void fraction measured simultaneously beside the total pressure measurement location. Neglecting the higher order terms, the turbulence intensity Tu was calculated as [21]

$$Tu = \sqrt{\frac{\frac{P_t'^2}{\rho_w^2 V^4} (1-C)C}{(1-C)\left(1 + \frac{C}{2}\right)}} \quad (2)$$

where Tu is defined as v'/V , v' is the velocity standard deviation, V is

the local time-averaged velocity, p_t' is the total pressure standard deviation, ρ_w is the water density, and C is the local time-averaged void fraction. (The derivation of Equation is detailed in Zhang et al. [21].) The accuracy of Equation on water-phase turbulence intensity estimate in bubbly flow was found to be linked with the uncertainty of dynamic calibration of the total pressure sensor as well as the error of using void fraction to approximate the pressure variations associated with the bubble impact on pressure sensor head [34].

3.3. Bubble clustering

The bubble re-grouping during their advection was investigated in terms of several particle clustering properties. First the typical bubble sizes were characterised using the bubble chord length, which was the time a bubble spent on the needle sensor tip multiplied by the local interfacial velocity. Two bubbles travelling one after the other were considered to form a one-dimensional bubble cluster when the interval time was smaller than the passage time of the leading bubble. That is, the following bubble was in the wake of the leading bubble, the wake size being the same as the leading bubble size. Such a clustering criterion is known as the near-wake criterion, adopted in air-water flow studies like Chanson et al. [22], Gualtieri & Chanson [23] and Wang et al. [24]. The clustering properties were analysed based on the binarised phase-detection signal.

3.4. Turbulent length and time scales

The typical size and lifetime of coherent eddy structures in the turbulent bubbly flow region were characterised in terms of the turbulent length and time scales in the streamwise direction. Performing an auto-correlation on the phase-detection signal, the normalised correlation coefficient R_{xx} decreases from unity with increasing time lag τ (Fig. 2a). The integration of the auto-correlation function $R_{xx}(\tau)$ till the first zero-crossing gives the auto-correlation time scale:

$$T_{xx} = \int_0^{\tau(R_{xx}=0)} R_{xx}(\tau) d\tau \quad (3)$$

Fig. 2a shows a definition sketch of T_{xx} based on present experimental data. The advection length scale L_{xx} is defined as

$$L_{xx} = |V| T_{xx} \quad (4)$$

The advection length scale reflects the average longitudinal

dimension of coherent eddy structures in which bubbles are advected. Its quantification is based on a single-point measurement over the lifetime of the structures. Simultaneous measurement at two locations separated by a longitudinal distance Δx provides another approach to the turbulent length scale. The maximum cross-correlation coefficient of the two-point measurement signals, $R_{xy,max}$, is a function of the separation distance Δx , and the integral turbulent length scale is defined as [25]

$$L_X = \int_0^{\Delta x(R_{xy,max}=0)} R_{xy,max} d(\Delta x) \quad (5)$$

The calculation of integral turbulent length scale is illustrated in Fig. 2b, where the maximum correlation coefficients corresponding to the sensor separation distances adopted in the present study are plotted. The integral turbulent length scale is a measure of the longitudinal dimension of bubble-advecting eddy structures based on the detection of a range of eddy sizes weighted by the maximum correlation. In the flow region with separate and additive advection and diffusion processes, it would be expected that the advection length scale and integral turbulent length scale are about equal in the longitudinal direction: $L_{xx} \approx L_X$.

The integral turbulent time scale is further calculated as

$$T_X = \frac{1}{L_X} \int_0^{\Delta x(R_{xy,max}=0)} R_{xy,max} T_{xy} d(\Delta x) \quad (6)$$

where T_{xy} is the cross-correlation time scale calculated as the integration of cross-correlation function from maximum to first zero-crossing (Fig. 2a).

4. Experimental flow conditions

Air-water flow measurements were performed for jet impact velocities greater than the critical onset velocity of air entrainment, V_e , which was identified as the jet velocity under which no bubble entrainment event occurred within a minimum interval of 5 minutes. With the present experimental setup, the critical onset velocity was observed for a range of water discharges (0.00175–0.00283 m³/s) and jet lengths (0.009–0.119 m). The observation results showed different onset velocities for experiments conducted with gradually increasing and decreasing jet impact velocities, implying a hysteresis process in term of the bubble inception conditions. Overall, the critical onset velocity was

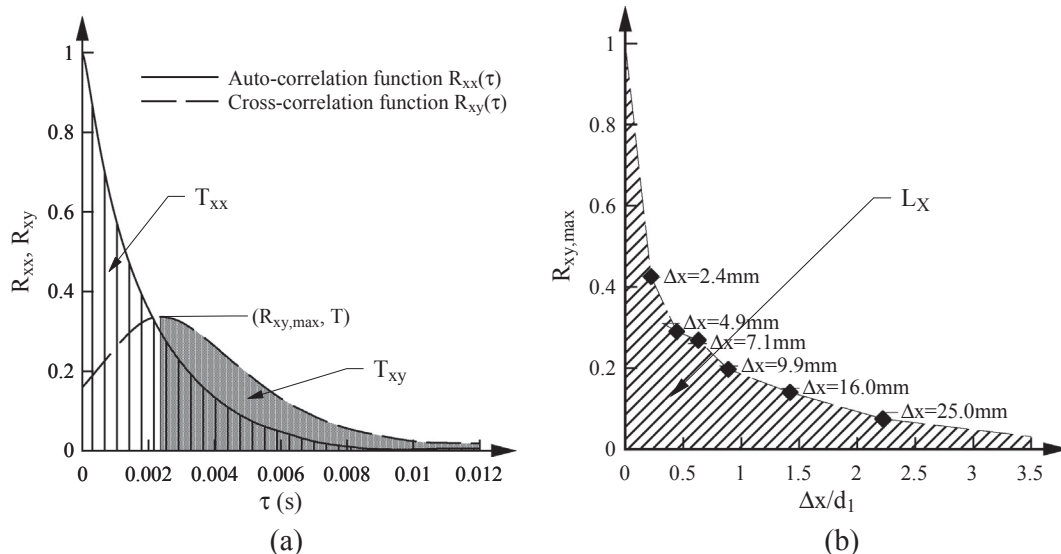


Fig. 2. Definition sketches of correlation time scales and integral turbulent length scale – Flow conditions: $V_1 = 2.5$ m/s, $x_1 = 0.1$ m, $x - x_1 = 0.04$ m: (a) Auto- and cross-correlation time scales; (b) Integral turbulent length scale.

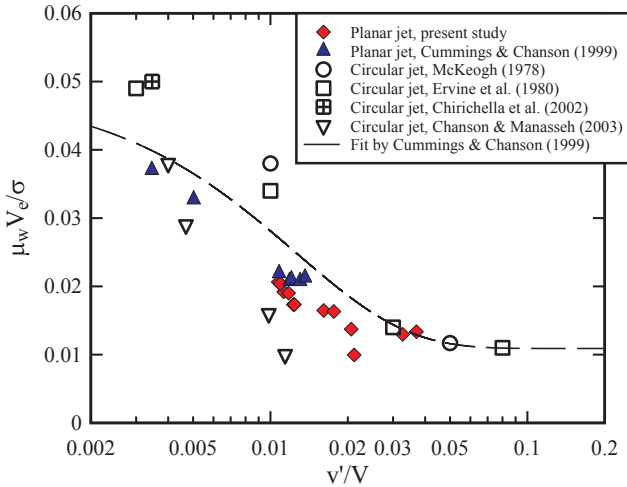


Fig. 3. Dimensionless inception velocity as a function of jet turbulence intensity, observed with increasing discharge and jet length.

observed between 0.9 and 1.7 m/s. Fig. 3 presents the dimensionless onset velocity as a function of the jet turbulence intensity, which was measured with a total pressure sensor in the clear-water region of the jet at the inception point. The present data are compared with the data of Cummings & Chanson [5] for planar jets and other observations on circular jets [26–28,14]. The different data sets showed a consistent trend of inception velocity decreasing with increasing jet turbulence level.

Three jet impact velocities greater than the critical inception velocity were investigated herein, i.e. $V_1 = 2.5, 4.0$ and 6.0 m/s, all for a fixed jet length $x_1 = 0.1$ m. The flow conditions are summarised in Table 1. All measurements were undertaken along the jet centreline.

The falling jet inflow conditions were characterised by relatively high disturbance level at the jet free-surface, and relatively high pre-entrainment of air bubbles into the jet. An acoustic detection of instantaneous jet surface position showed developing free-surface fluctuations along the falling jet centreline. The standard deviation of jet thickness fluctuations was about 15% of the mean jet thickness d_1 at the impingement point ($x_1 = 0.1$ m) for all jet velocities. The development of jet surface disturbance induced interfacial air entrainment, characterised by a streamwise broadening of air-water mixing layer where the void fraction was typically between 0.1 and 0.9. The thickness of such surface mixing layer reached the order of the jet thickness at $x_1 = 0.1$ m. In the highly-aerated jet, the flow turbulence level at impingement was estimated using Eq. (2), yielding a free-stream turbulence intensity between 4% and 8% for the investigated jets (Table 1).

5. Results (1): air entrainment by turbulent shear flow

5.1. Void fraction, bubble count rate and interfacial velocity

For all tested jet impact velocities, a bubble cloud formed underneath the impingement point. The air-water flow pattern was characterised with the spatial distributions of time-averaged void fraction C

Table 1
Experimental flow conditions for air-water flow measurements.

Q (m ³ /s)	d ₀ (m)	V ₀ (m/s)	x ₁ (m)	d ₁ (m)	V ₁ (m/s)	Fr (-)	Re (-)	We (-)	Tu ₁ (-)
0.0067	0.012	2.1	0.1	0.0100	2.5	8.2	2.7×10^4	820	0.075
0.0121	0.012	3.7	0.1	0.0112	4.0	12.1	5.0×10^4	2480	0.050
0.0189	0.012	5.8	0.1	0.0117	6.0	17.7	7.9×10^4	5820	0.045

Notes: Q: water discharge; d₀: jet thickness at nozzle; V₀: jet velocity at nozzle; x₁: jet length; d₁: jet thickness at impingement; V₁: jet impact velocity; Fr: jet Froude number, $Fr = V_1 / (gd_1)^{0.5}$; Re: jet Reynolds number, $Re = \rho_w V_1 d_1 / \mu_w$; We: jet Weber number, $We = \rho_w V_1^2 d_1 / \sigma$; Tu₁: inflow free-stream turbulence intensity.

and bubble count rate F , as illustrated in Fig. 4a and b for the largest tested jet velocity $V_1 = 6$ m/s. Fig. 4c shows the time-averaged longitudinal interfacial velocity distributions for the same jet conditions. In Fig. 4, both data measured in the falling jet ($x - x_1 < 0$) and plunging pool ($x - x_1 > 0$) are included, and the presented data are the ensemble-average of the data of six phase-detection probes with different Δx .

The contour plots in Fig. 4 shows that the highest void fraction was observed just below the impingement point (Fig. 4a). The spread of bubble cloud in both longitudinal and horizontal directions indicated a diffusive advection of air bubbles in the plunging pool. For a given void fraction, the bubble count rate was proportional to the total air-water interfacial area. The maximum bubble count rate was found to be located where the vortex shedding in the shear layer interacted with the high-speed jet core (Fig. 4b). The vortical structures in the shear layer were visualised by the air bubbles they carried. The vortex size increased and its formation frequency decreased with increasing jet velocity. Fig. 4b also highlights the high air-water interfacial frequency in the falling jet prior to the impingement, due to the jet free-surface fluctuations and pre-aeration.

The interfacial velocity distributions in Fig. 4c show the transition from positive velocity next to the jet support to slightly negative velocity in the ambient water where the bubbles were driven upwards by buoyancy. The longitudinal broadening of the transition region was consistent with the observation in a free-shear flow. The interfacial velocity data compared well with the flow velocity deriving from the total pressure measurement in the jet core region (data not shown). In the far end of the pool, the kinetic pressure was negligible and the total pressure equalled to the static pressure related to the local depth.

The cross-sectional distributions of void fraction, dimensionless bubble count rate and longitudinal velocity data are detailed in Fig. 5 at a given depth $x - x_1 = 0.08$ m for all three impact velocities. Comparing the data for different jet impact velocities, similar profile shapes were shown for the respective parameters. The void fraction and bubble count rate both showed unimodal distributions, with the maximum void fraction and bubble count rate increasing with increasing jet impact velocity. These corresponded to the enhancement of air entrainment and air-water mixing in a faster plunging jet. A larger impact velocity also yielded a larger penetration depth of entrained bubbles. That is, the maximum interfacial velocity was slightly higher at a given depth and it took a longer distance to decrease to zero for a larger impact velocity. In Fig. 5, the void fraction data are compared with the solution of the air bubble advective diffusion equation (Eq. (7)), and the velocity data are compared with the solution of monophasic free-shear flow velocity field (Eq. (8)), both for $V_1 = 4$ m/s:

$$C = C_{\max} \left(\exp \left(-\frac{1}{4D^\#} \left(\frac{y - Y_{C_{\max}}}{d_1} \right)^2 \right) + \exp \left(-\frac{1}{4D^\#} \left(\frac{y + Y_{C_{\max}}}{d_1} \right)^2 \right) \right) \quad (7)$$

$$\frac{V - V_{\text{recirc}}}{V_{\max} - V_{\text{recirc}}} = \frac{1}{2} \left(1 + \text{erf} \left(\frac{K(y - Y_{0.5})}{x - x_1} \right) \right) \quad (8)$$

where C and V are respectively the void fraction and longitudinal velocity at a given position ($(x - x_1)/d_1, y/d_1$), C_{\max} is the local maximum void fraction, $Y_{C_{\max}}$ is the normal position of C_{\max} , $D^\#$ is the

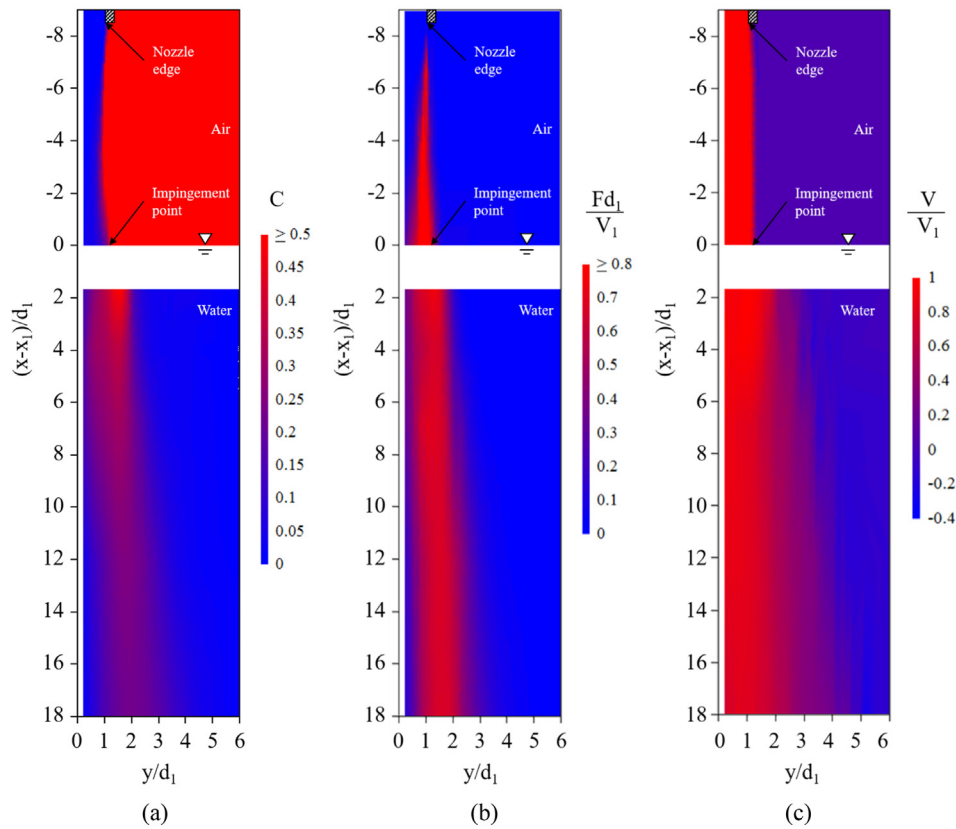


Fig. 4. Contour maps of (a) time-averaged void fraction, (b) dimensionless bubble count rate and (c) longitudinal interfacial velocity distributions in falling jet and plunging pool – Flow conditions: $Q = 0.0189 \text{ m}^3/\text{s}$, $x_1 = 0.1 \text{ m}$, $V_1 = 6.0 \text{ m/s}$.

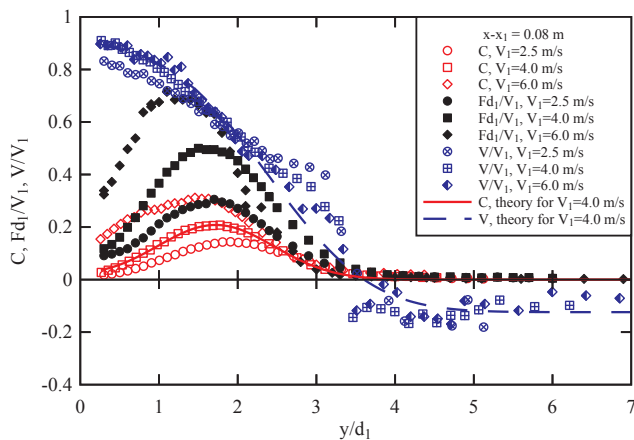


Fig. 5. Cross-sectional distributions of void fraction, dimensionless bubble count rate and longitudinal velocity in plunging pool ($x - x_1 = 0.08 \text{ m}$), with comparison to theoretical solutions for void fraction (Eq. (7)) and interfacial velocity (Eq. (8)).

dimensionless cross-sectional average bubble diffusivity; V_{\max} is the maximum longitudinal velocity next to the jet support, V_{recirc} is the mean recirculation velocity, $Y_{0.5}$ is the position of maximum velocity gradient, i.e. $Y_{0.5} = y((V_{\max} + V_{\text{recirc}})/2)$, and K is a coefficient derived from the assumption of constant eddy viscosity at a given cross-section: $v_t = V_1(x - x_1)/(4K^2)$.

Eqs. (7) and (8) compared well with the experimental data (Fig. 5). The characteristic parameters like C_{\max} , V_{\max} , Y_{Cmax} and $Y_{0.5}$ were calibrated against the experimental data, and their longitudinal variations are shown in Fig. 6, with comparison to previous studies [6,29]. Despite differences between jet flow conditions, the data showed overall

consistent distributions for each parameter, namely, streamwise decrease in the maximum void fraction C_{\max} and maximum velocity V_{\max}/V_1 and increase in the characteristic positions Y_{Cmax}/d_1 and $Y_{0.5}/d_1$.

5.2. Turbulence intensity in bubbly flow

The presence of air bubbles made direct measurement of water-phase turbulence intensity difficult in the plunging pool. Herein the turbulence intensity Tu was approximated using Eq. (2) based on simultaneous measurements of void fraction, velocity and total pressure fluctuations. Typical results are presented in Fig. 7 for three jet impact velocities at the same longitudinal position $x - x_1 = 0.14 \text{ m}$. The corresponding void fraction profiles are plotted for comparison.

Most sample points showed a turbulence intensity between 0.05 and 0.6. A typical cross-sectional distribution exhibited a maximum turbulence intensity between $Tu = 0.4$ and 0.7 at a normal position between $y/d_1 = 1.8$ and 2.7 for the present flow conditions. The peak turbulence intensity was related to the presence of recirculating vortical structures in the shear layer, where the instantaneous velocity shifted between positive and negative, and the time-averaged velocity was small. For a given plunging jet, the longitudinal variation trend of turbulence intensity was not obvious. It was affected by both streamwise development of large-size vortices and dissipation of microscopic eddy structures, while the influence of air bubble concentration also changed with increasing depth. Fig. 7 suggests a smaller relative velocity fluctuation for a larger jet impact velocity. This finding may require further data verification because, for a faster jet with higher local void fraction, the approximation of turbulence intensity using Eq. (2) was subject to larger uncertainties associated with the bubble impact on total pressure readings. Other suppositions of Eq. (2) included assumption of isotropic turbulence and irrotational flow, and ignorance of higher order turbulence intensities.

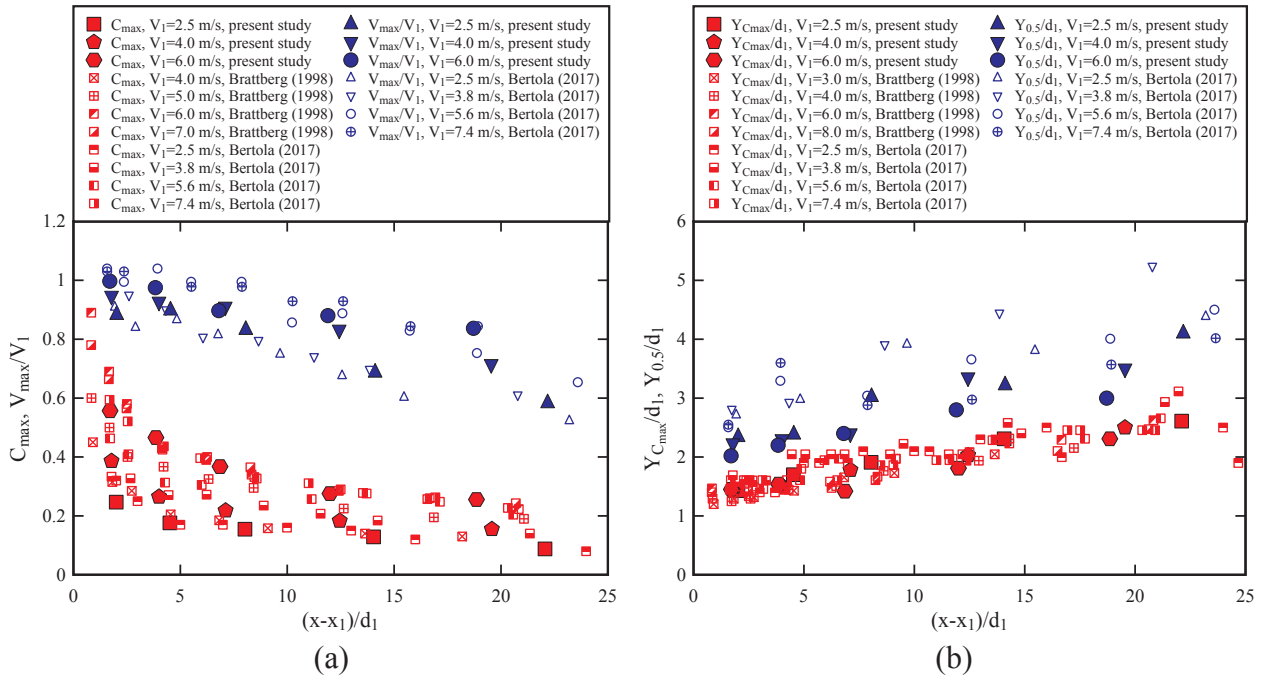


Fig. 6. Longitudinal evolution of maxima in void fraction, maximum longitudinal velocity and corresponding normal distances from the jet support, with comparison to data of Brattberg & Chanson [6] and Bertola et al. [29].

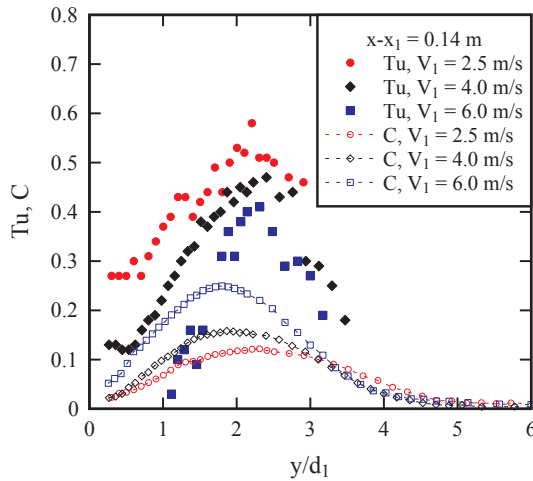


Fig. 7. Water-phase turbulence intensity in bubbly flow for three jet impact velocities at the same longitudinal position $x - x_1 = 0.14$ m, with comparison to void fraction data.

6. Results (2): bubble-turbulence interplay

6.1. Bubble size distributions

The bubble size in the shear flow was sensitive to the turbulence development and dissipation. Herein the typical bubble size in the plunging pool was characterised using the bubble chord length (Section 3.3). Fig. 8 shows the probability distributions of bubble chord length at four depths below the impingement point, all at the normal positions where the bubble count rate reached maximum ($y = Y_{Fmax}$). The probability density function (PDF) was calculated for bubble chord lengths grouped with 1 mm interval, except for large chord lengths greater than 8 mm being regrouped into a single bin (> 8 mm). The results are compared between two jet impact velocities $V_1 = 2.5$ and 6.0 m/s.

At the given locations, Fig. 8 shows that the majority of bubbles had

chord lengths smaller than 3 mm. For each impact velocity, the percentage of smaller bubbles increased with increasing depth for $0.02 \text{ m} < x - x_1 < 0.22 \text{ m}$, as a result of large bubbles breaking into small ones by shear stress. For example, for $V_1 = 6.0$ m/s, the proportion of submillimeter bubbles increased from 16% to 43% at $x - x_1 = 0.02$ m to 0.22 m, while that of large bubbles (chord length > 8 mm) decreased from 24% to 5%. This suggested a longitudinal decrease in average bubble size, and the variance was more significant for a larger jet velocity.

6.2. Bubble clustering

In the presence of macroscopic turbulent structures larger than the bubble dimensions, the bubble distribution and convection were not random processes. A form of bubble-turbulence interplay was the bubble regrouping, or, bubble clustering. Herein, one-dimensional bubble clusters were identified based upon the near-wake criterion (Section 3.3), and the bubble clustering behaviour was investigated in terms of cluster count rate F_{clu} defined as the number of clusters per second, cluster size N_{clu} defined as the average number of bubbles per cluster, and cluster proportion P_{clu} defined as the percentage of bubbles in clusters relative to the total number of bubbles.

Fig. 9a presents typical dimensionless distributions of cluster count rate for three jet impact velocities at the same depth $x - x_1 = 0.14$ m, with comparison to the bubble count rate distributions. The average cluster size and cluster proportion are shown in Fig. 9b for the same flow conditions. The bubble and bubble cluster count rates showed similar unimodal profile shapes, with $F_{clu} < F$. The present data suggested a relationship between the maximum cluster count rate and maximum bubble count rate:

$$\frac{F_{clu,max} d_1}{V_1} = 0.205 \left(\frac{F_{max} d_1}{V_1} \right)^{1.072} \quad (9)$$

The cluster size and cluster proportion data showed bell-shape distributions close to the typical void fraction profile shape. Fig. 9c plots the maximum values of cluster count rate, cluster size and cluster proportion in all cross-sections as functions of the longitudinal position.

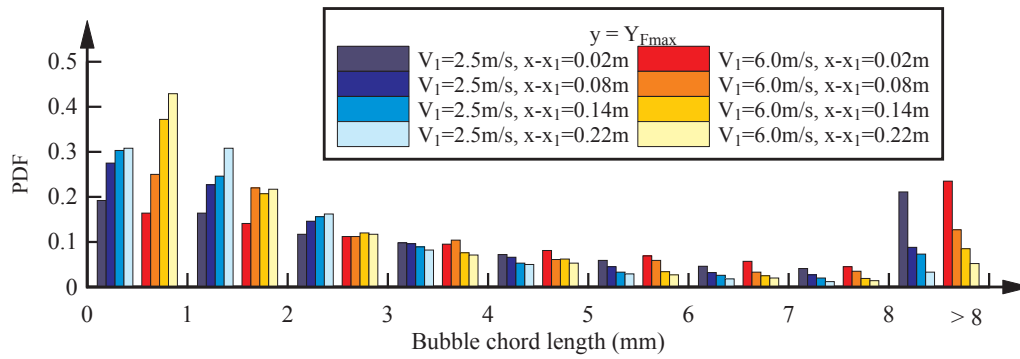


Fig. 8. Probability density functions of bubble chord length at the location of maximum bubble count rate and four longitudinal positions – comparison between jet impact velocities.

The corresponding normal positions of the maxima are shown in Fig. 9d and compared with the linear fits of the characteristic positions Y_{Cmax} and Y_{Fmax} where the maximum void fraction and bubble count rate occurred. The data suggested most intensive bubble clustering events taking place in the shear flow region. For example, at immediately

below the impingement point, over 50% of the entrained bubbles were involved in the formation of bubble clusters, with an average of 2.4 bubbles per cluster for $V_1 = 2.5$ m/s and 2.7 bubbles per cluster for $V_1 = 6.0$ m/s. Both the percentage of clustered bubbles and the average number of bubbles in each cluster decreased with increasing depth. As

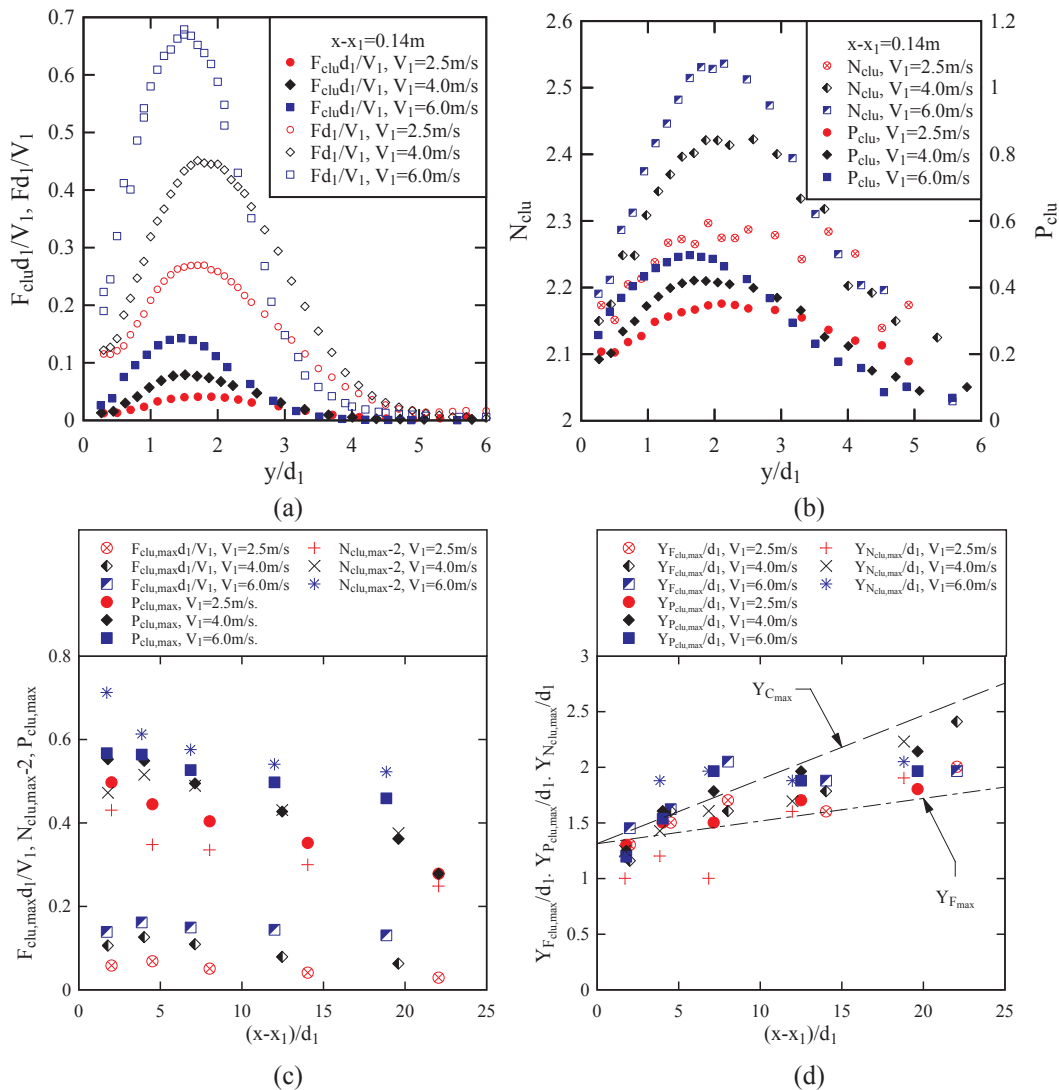


Fig. 9. Bubble clustering properties: (a) Cross-sectional distributions of dimensionless bubble cluster count rate, with comparison to bubble count rate; (b) Cross-sectional distributions of average cluster size and cluster proportion; (c) Longitudinal distributions of maxima in cluster count rate, cluster size and cluster proportion; (d) Longitudinal distributions of normal positions for maximum cluster count rate, cluster size and cluster proportion, with comparison to the linear fit of positions for maximum void fraction and bubble count rate.

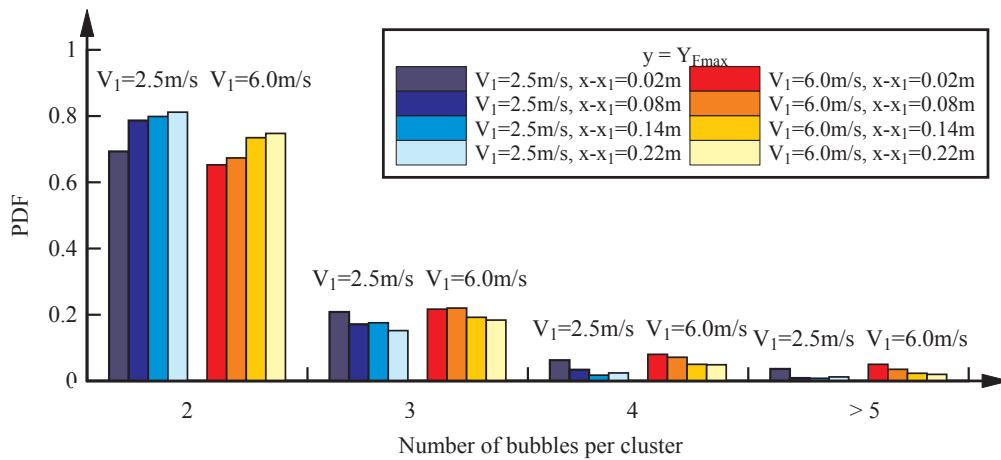


Fig. 10. Probability density functions of cluster size at the location of maximum bubble count rate and four longitudinal positions – comparison between jet impact velocities.

bubbles diffused and turbulent structures dissipated during streamwise advection, large bubble clusters tended to lose bubbles or break down into smaller clusters, and the decreasing bubble size (Fig. 8) further weakened the interplay between neighbouring bubbles.

A further insight into the cluster size was the probability distribution of clusters of different number of bubbles. Fig. 10 shows the PDFs of clusters consisting of two, three, four and no less than five bubbles. The results were collected at the same longitudinal and normal positions as in Fig. 8, and are compared between $V_1 = 2.5$ and 6.0 m/s. The data highlighted a predominant proportion of small clusters formed by two bubbles travelling one after the other. The percentage of two-bubble clusters increased from 70% to 80% over a longitudinal distance of $10d_1$ for $V_1 = 2.5$ m/s. This percentage was slightly smaller for $V_1 = 6.0$ m/s, increasing from 65% to 75% over the same distance. Correspondingly, the proportion of larger clusters consisting of three, four and more bubbles was consistently smaller for a lower jet impact velocity and decreased with increasing longitudinal distance. The PDFs of cluster size were comparable to the results from a study of hydraulic jump where the turbulent structures also tended to group bubbles into clusters during the horizontal bubble advection [24]. The vanishing large clusters ($N_{clu} > 5$) along the turbulent shear flow could be an indicator of decoupling between the convected bubbles and turbulent structures.

6.3. Bubbly flow turbulent length and time scales

In a plunging jet with a turbulent shear layer developing between the jet core and surrounding water, a broad range of eddy structures formed and were advected in the bubbly flow region, most of which interacted with the entrained air bubbles [30]. Two measures of characteristic size of those turbulent structures responsible to the bubble advection were compared herein, namely, the advection length scale L_{xx} and the integral turbulent length scale L_x , both in terms of the longitudinal dimensions. The former was calculated based on the average lifetime of the coherent bubbly structures and the average interfacial velocity, while the latter was based on averaging (integration) of a range of eddy sizes weighted by a normalised correlation factor.

Fig. 11 shows both turbulent length scale distributions for three jet impact velocities. The results showed some interesting difference between the two length scales in the turbulent shear region, i.e. between the jet support and approximately the position of $Y_{0.5}$. The integral turbulent length scale L_x showed a local maximum value in the order of d_1 near the jet support ($y/d_1 < 1$), which decreased in the streamwise direction. This maximum integral length scale corresponded to the downstream convection of aerated jet core structures, which dissipated rapidly for a slower impinging jet and maintained over a longer

distance for a faster jet. Such jet core structures, particularly the large-size ones, were detected by the simultaneous measurements at two longitudinal locations (L_x) but was missed by the single-point measurement for a given duration (L_{xx}). On the other hand, there were some occasions where a maximum advection length scale L_{xx} was shown in the shear layer ($1 < y/d_1 < 4$). A secondary peak in integral length scale L_x was sometimes observed at the same location (not always distinctive). These local maxima could be better seen in terms of auto-correlation time scale T_{xx} and integral turbulent time scale T_x in Fig. 12. The local peak length and time scales in the shear layer were associated with the presence of large-size vortical structures in the form of Kelvin-Helmholtz instabilities. The transport of air bubbles in such well-structured vortices yielded an increase in both temporal and spatial correlations of the phase-detection signals, thus resulting in larger turbulent scales. For the data in Fig. 12, the normal positions of maximum auto-correlation and integral time scales were documented, which were found to be very close to the position of maximum velocity gradient $Y_{0.5}$. Beyond this position ($y > Y_{0.5}$), the two turbulent length scales L_{xx} and L_x became similar and both decreased to zero in the surrounding water where no eddy structures existed.

Overall, the results suggested typical longitudinal dimensions of coherent bubbly structures between $0.1d_1$ and $1.5d_1$, larger in the jet core and close to the impingement while smaller in the surrounding and deep water. The lifetime of the structures was typically in the order of 10^{-3} s and reached maximum in the turbulent shear layer. A higher jet impact velocity yielded larger turbulent length and time scales at a given position. The advection length scale based on temporal correlation and integral turbulent length scale based on spatial correlation showed different distributions in the jet core region, implying a complex coupling between the bubble advection and diffusion processes.

7. Discussion: Longitudinal turbulent length scales in hydraulic jump and plunging jet

A classic hydraulic jump is a horizontal supported plunging jet, as sketched in Fig. 13 [33]. Although a turbulent shear layer also forms downstream of the impingement point, the bubble transport in a hydraulic jump is not identical as in a plunging jet, because of the different gravity direction and free-surface behaviour. The inflow free-surface disturbance is thought to play a less critical role in a hydraulic jump in terms of influencing the air entrainment at the impingement point, because the vertical surface fluctuations are constrained by the gravity. On the other hand, the free-surface of hydraulic jump roller is highly breaking and fluctuating, involving recirculating motions and secondary air entrainment [31,32]. The aerated shear flow beneath the jump roller is consistently de-aerated through the roller free-surface till

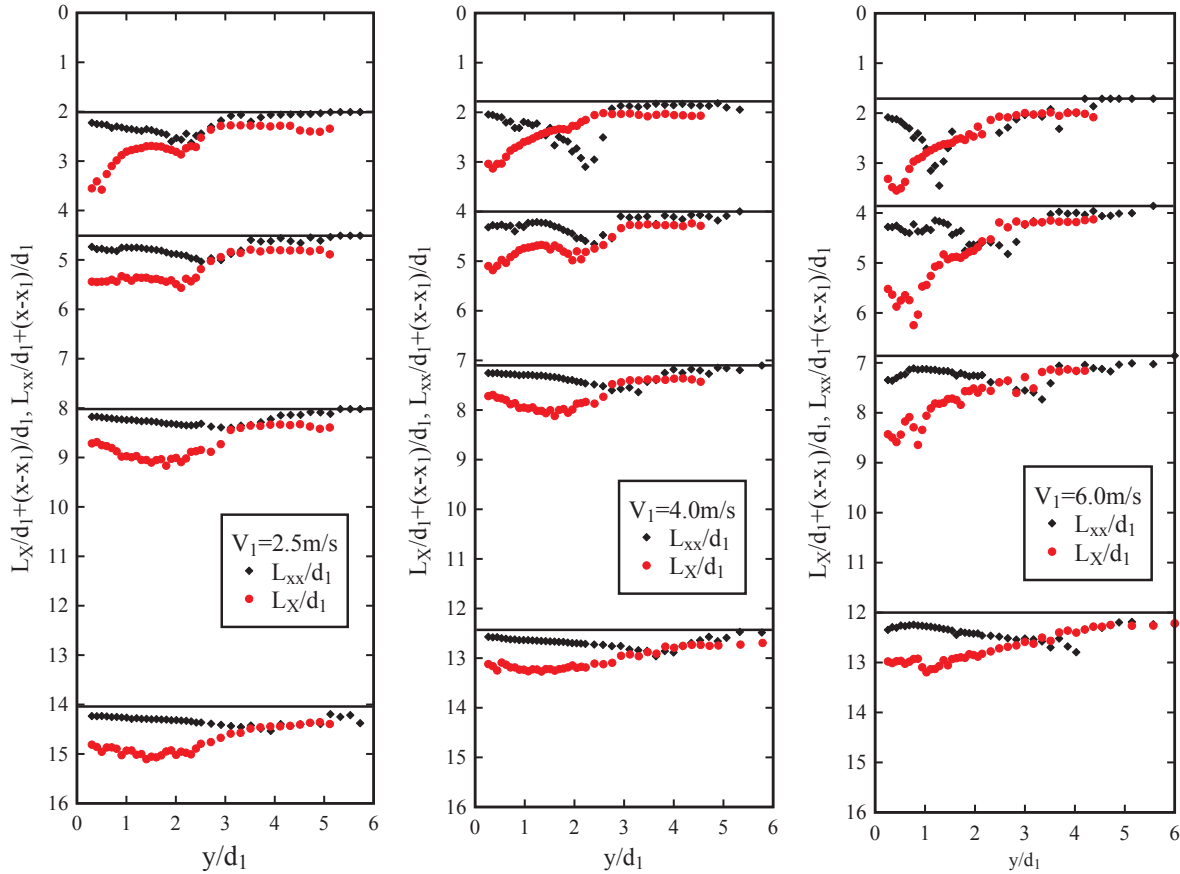


Fig. 11. Longitudinal advection length scale and integral turbulent length scale in plunging pool. From left to right: $V_1 = 2.5$ m/s, 4.0 m/s and 6.0 m/s.

the end of air-water flow region, while in a plunging jet, de-aeration of shear flow was only observed for a highly pre-aerated jet within a short distance below the impingement point [29]. Wang et al. [30] reported the longitudinal advection and integral turbulent length scales in a horizontal hydraulic jump for $Fr = 7.5$ and $Re = 6.8 \times 10^4$. Wang & Murzyn [34] further included a test case with flow conditions closer to the present plunging jet conditions, i.e., with the same initial inflow thickness $d_0 = 0.012$ m and similar impact velocity $V_1 = 2.67$ m/s. The hydraulic jump flow conditions are summarised in Table 2.

Fig. 14 shows a comparison of the spatial distributions of advection and integral turbulent length scales (L_{xx} & L_x) in the bubbly flow regions of hydraulic jump and plunging jet. Note that the hydraulic jump had larger impinging velocity and Reynolds number. The data showed comparable longitudinal dimensions of the turbulent structures for the two flow types, which were in the order of inflow thickness d_1 . Similar to the present observation in the jet core region, different L_{xx} and L_x were also obtained in hydraulic jump downstream of the jump toe, with $L_{xx} < L_x$ in the high-speed area between the channel bed and shear layer. In a hydraulic jump, the large turbulent structures seemed to dissipate more rapidly, i.e. over a shorter distance in the horizontal direction, before the advection and integral length scales became identical, implying well-separated bubble advection and diffusion processes in the relatively calm and quasi-uniform downstream flow. The most distinctive difference between the two flow types existed at the jump roller free-surface, where the large-scale surface motions led to large turbulent length scales and $L_{xx} > L_x$. In comparison, the turbulent length scales in the plunging pool dropped to zero in the quasi-still water.

The turbulent length and time scales may further allow for an approximation of turbulent viscosity in the air-water flow, in a form of $\nu_t = L_x^2/T_x$. Herein the relative value of turbulent viscosity to bubble

diffusivity was evaluated as the Schmidt number:

$$Sc = \frac{\nu_t}{D_t} \quad (10)$$

where the bubble diffusivity D_t was assumed to be constant across the turbulent shear flow at a given longitudinal position $(x - x_1)/d_1$, independent of the normal position y/d_1 . For both plunging jet and hydraulic jump, D_t was derived from Eq. (7) by $D^\# = D_t/(V_1 d_1)$, and $D^\#$ was given by the best fit of Eq. (7) to the experimental data. Fig. 15 plots the Schmidt number in a given cross-section of hydraulic jump ($x - x_1 = 0.15$ m) and plunging jet ($x - x_1 = 0.14$ m), with comparable inflow thicknesses, impact velocities and Froude numbers. The void fraction profiles are also included for reference. For both flow types, the Schmidt number in the high-speed impinging flow region ($0 < y < Y_{Cmax}$) was contrastively higher than on the other side of the shear layer ($y > Y_{Cmax}$). The air-water flow in the high-Schmidt-number region was predominantly driven by the inertial force of the high-momentum impinging flow, and the bubble diffusion was less important compared to the streamwise bubble advection by the turbulent flow. For comparable impinging flow conditions, the streamwise turbulent convection in a plunging jet was enhanced by the gravity acting in the flow direction, while in a hydraulic jump, the gravity/buoyancy affected the bubble diffusion perpendicular to the flow direction. This was reflected by the plunging jet Schmidt number almost double of the hydraulic jump Schmidt number for $y < Y_{Cmax}$. For $y > Y_{Cmax}$, the Schmidt number in hydraulic jump became higher than in plunging jet, because large turbulent structures formed in the hydraulic jump free-surface recirculation region, whereas any eddy structures would dissipate rapidly in the plunging pool.

The turbulent viscosity is a key parameter for many numerical turbulent models. However, there are little experimental characterisation of turbulent viscosity in a gas-liquid two-phase flow. The present

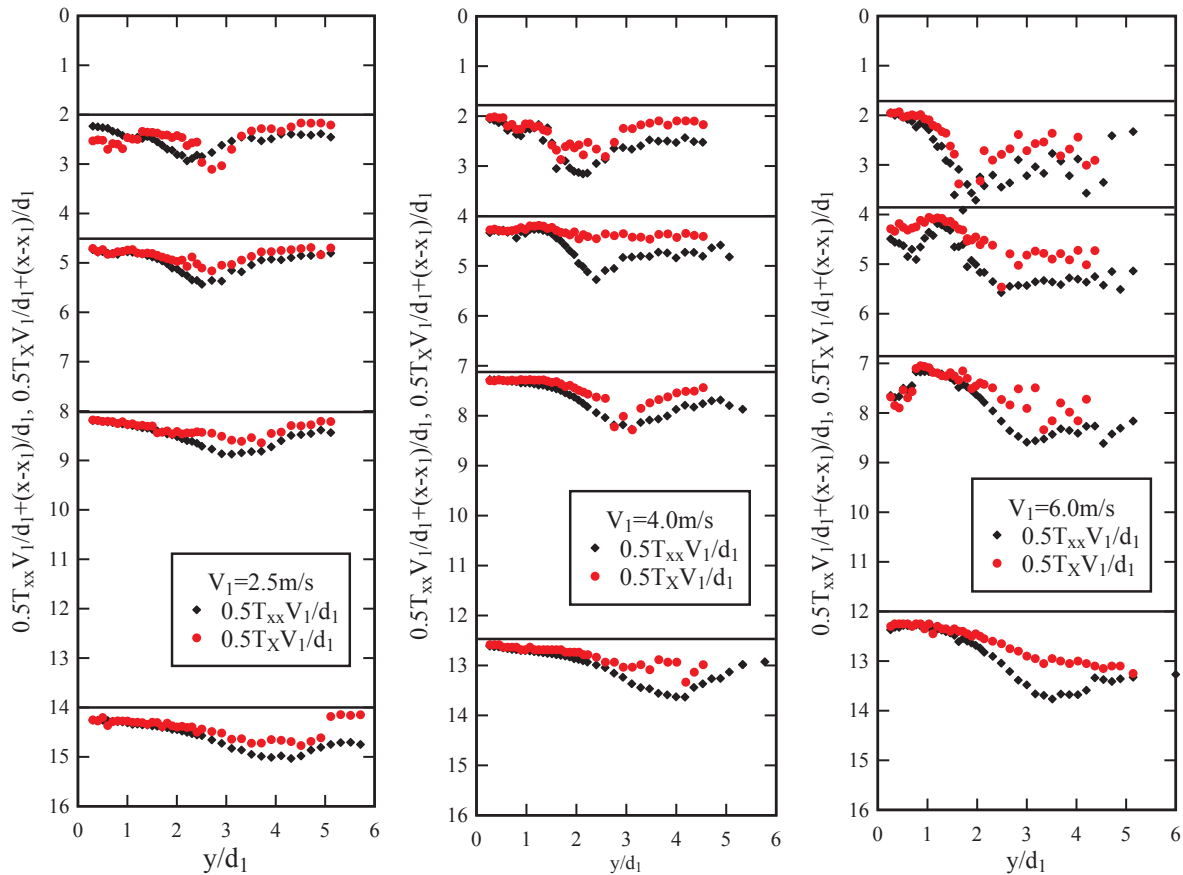


Fig. 12. Longitudinal auto-correlation time scale and integral turbulent time scale in plunging pool. From left to right: $V_1 = 2.5$ m/s, 4.0 m/s and 6.0 m/s.

results may initiate some discussion on the relative effects of turbulent viscosity to diffusivity.

8. Conclusion

The air-water flow in a two-dimensional supported plunging jet was investigated using intrusive phase-detection probes. A total of six dual-tip probes were used with identical needle sensors but different spacing between leading and trailing sensors. Most air-water flow properties were presented as the ensemble-average of the data of six probes. The effects of jet impact velocity were systematically tested for $V_1 = 2.5, 4.0$ and 6.0 m/s with a fixed jet length $x_1 = 0.1$ m. The jet impact velocities were greater than the onset velocity for air entrainment which was observed between 0.9 and 1.7 m/s with the present experimental setup as a function of the jet turbulence level.

The inflow jet conditions were characterised with relatively large jet disturbance and pre-aeration. The spatial distribution and evolution of

void fraction, bubble count rate and interfacial velocity in the plunging pool indicated the downstream bubble transport being an advective diffusion process. The air entrainment and air-water mixing were enhanced by an increasing impact velocity. The void fraction and velocity distributions could be modelled with the analytical solutions of bubble diffusion and shear flow velocity equations, with the impingement point being the point source of air entrainment and velocity discontinuity. The turbulence intensity in the bubbly flow region was quantified based on void fraction and total pressure fluctuation measurements. The results ranged between 0.05 and 0.6 and reached a maximum within the turbulent shear layer.

The bubble-turbulence interplay was characterised in terms of bubble clustering based on a near-wake criterion and turbulent length and time scales of the coherent bubbly flow structures. The clustering analysis showed intensive bubble regrouping in the shear flow region, although more than half of the clusters consisted of only two neighbouring bubbles. The cluster count rate, average cluster size and

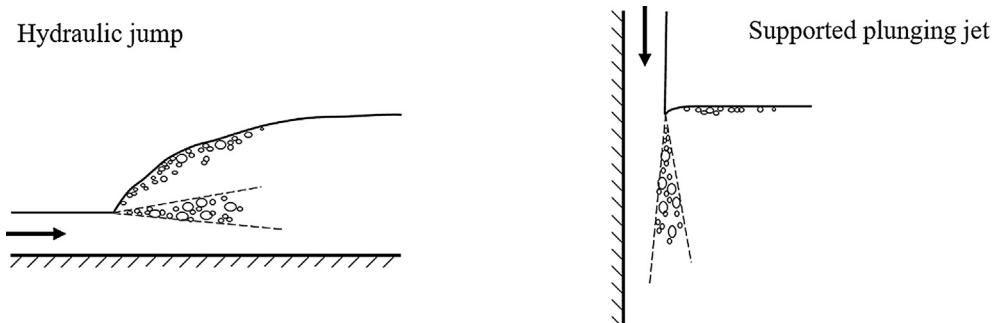


Fig. 13. Sketches of two-dimensional hydraulic jump and supported plunging jet.

Table 2
Hydraulic jump flow conditions for turbulent length scale measurements in Wang et al. [30] and Wang & Murzyn [34].

	Q (m ³ /s)	B (m)	d ₀ (m)	x ₁ (m)	d ₁ (m)	V ₁ (m/s)	Fr (-)	Re (-)	x - x ₁ (m)
PJ	0.0067	0.269	0.012	0.10	0.0100	2.50	8.2	2.7 × 10 ⁴	0.02, 0.045, 0.08, 0.14, 0.22
HJ	0.0172	0.5	0.012	0.50	0.0129	2.67	7.5	3.4 × 10 ⁴	0.15
HJ	0.0333	0.5	0.020	0.83	0.020	3.33	7.5	6.6 × 10 ⁴	0.083, 0.167, 0.25, 0.375, 0.5

Notes: PJ: plunging jet; HJ: hydraulic jump; Q: water discharge; B: channel width; d₀: gate/nozzle opening; x₁: inflow length; d₁: inflow thickness at impingement; V₁: inflow velocity; Fr: inflow Froude number, $Fr = V_1/(gd_1)^{0.5}$; Re: inflow Reynolds number, $Re = \rho_w V_1 d_1 / \mu_w$.

proportion of clustered bubbles all reached maxima in the shear layer. For a larger jet impact velocity, more bubbles were involved in the formation of a greater number of large-size clusters. The large clusters broke down into small ones with streamwise dissipation of turbulent structures.

Two turbulent length scales were derived and compared, namely, the advection length scale based on a single-point temporal correlation and the integral turbulent length scale based on a multi-point spatial correlation. The corresponding time scales showed similar profile shapes with typical eddy structure lifetime in the order of 10⁻³ s. Differences between the length scales were observed in the high-speed jet core region, where the characteristic longitudinal dimension of eddy structures could range from 0.1d₁ to d₁, decreasing with increasing longitudinal distance from the impingement point. Different advection and integral length scales were also observed in horizontal hydraulic jumps, implying that the bubble advection and diffusion were not separate processes. The integral turbulent length and time scales provided an estimate of turbulent viscosity, of which the relative effects to bubble diffusivity might be evaluated as the Schmidt number. In the high-speed flow region, the Schmidt number in plunging jet was larger than that in hydraulic jump because of the gravity force acting in the flow direction enhancing the advection of bubbly vortices. In addition to the gravity, the bubble convection in the turbulent shear flow was also influenced by the presence of breaking free-surface in a hydraulic

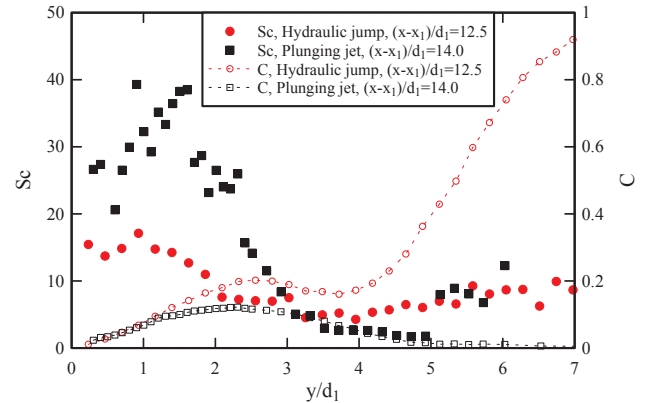


Fig. 15. Schmidt number $Sc = \nu_t/D_t$ in a cross-section of bubbly flow region in hydraulic jump ($x - x_1 = 0.15$ m) and plunging jet ($x - x_1 = 0.14$ m), with comparison to void fraction distribution – Hydraulic jump flow conditions: $d_1 = 0.0129$ m, $V_1 = 2.67$ m/s, $Fr = 7.5$, $Re = 3.4 \times 10^4$; Plunging jet flow conditions: $d_1 = 0.00995$ m, $V_1 = 2.50$ m/s, $Fr = 8.2$, $Re = 2.7 \times 10^4$.

jump compared to in a plunging jet. It is recommended that the quantitative characterisation of bubble-turbulence interplay should be considered in the verification of numerical modelling of highly-aerated

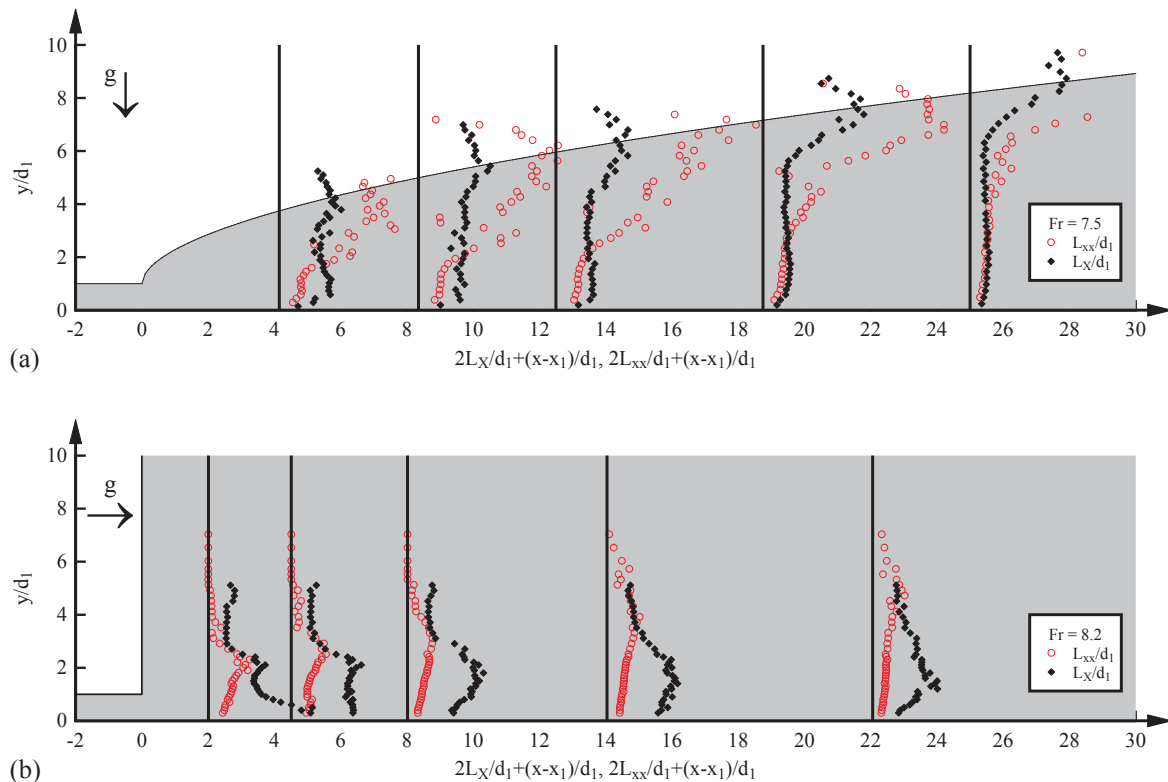


Fig. 14. Advection length scale and integral turbulent length scale in (a) hydraulic jump and (b) plunging jet – Hydraulic jump flow conditions: $d_1 = 0.02$ m, $V_1 = 3.33$ m/s, $Fr = 7.5$, $Re = 6.6 \times 10^4$; Plunging jet flow conditions: $d_1 = 0.00995$ m, $V_1 = 2.50$ m/s, $Fr = 8.2$, $Re = 2.7 \times 10^4$.

turbulent flow.

Acknowledgement

The authors thank Dr. Gangfu Zhang (The University of Queensland) for providing programming assistance. They thank Dr. Daniel Valero's valuable comments on data analysis. The phase-detection probes were manufactured by Jason Van Der Gevel (The University of Queensland). The financial support of the Australian Research Council (ARC DP120100481) and of The University of Queensland is acknowledged.

References

- [1] D.A. Ervine, E.M. Elsayy, The effect of falling nappe on river aeration, in: Proc. 16th IAHR Congress, Sao Paulo, Brazil, vol. 3 (paper C45), 1975, pp. 390–397.
- [2] J.N. Ginoux (Ed.), *Two-Phase Flow and Heat Transfer*, McGraw Hill/Hemisphere, 1978.
- [3] N.H. Thomas, T.R. Auton, K. Sene, J.C.R. Hunt, Entrapment and transport of bubbles by transient large eddies in multiphase turbulent shear flows, in: Proc. Intl. Conf. on Physical Modelling of Multiphase Flow, BHRA Fluid Eng., Coventry, UK, 1983, pp. 169–184.
- [4] A. Bin, Gas entrainment by plunging liquid jets, *Chem. Eng. Sci.* 48 (21) (1993) 3585–3630.
- [5] P. Cummings, H. Chanson, An experimental study of individual air bubble entrainment at a planar plunging jet, *Chem. Eng. Res. Des. Trans. IChemE, Part A* 77 (A2) (1999) 159–164.
- [6] T. Brattberg, H. Chanson, Air entrainment and air bubble dispersion at two-dimensional plunging water jets, *Chem. Eng. Sci.* 53 (24) (1998) 4113–4127, [http://dx.doi.org/10.1016/S0009-2509\(98\)80004-3](http://dx.doi.org/10.1016/S0009-2509(98)80004-3).
- [7] K. Kiger, J. Duncan, Air-entrainment mechanisms in plunging jets and breaking waves, *Annu. Rev. Fluid Mech.* 44 (2012) 563–596.
- [8] P.J. Roache (Ed.), *Verification and Validation in Computational Science and Engineering*, Hermosa Publishers, Albuquerque NM, USA, 1998, p. 446.
- [9] P.J. Roache, Perspective: validation – what does it mean? *J. Fluids Eng., ASME* 131 (March) (2009) 034503.
- [10] J. Ma, A.A. Oberai, R.T. Lahey, D.A. Drew, Modeling air entrainment and transport in a hydraulic jump using two-fluid RANS and DES turbulence models, *Heat Mass Transf.* 47 (8) (2011) 911–919.
- [11] J. Ma, A.A. Oberai, D.A. Drew, R.T. Lahey, A two-way coupled polydispersed two-fluid model for the simulation of air entrainment beneath a plunging liquid jet, *J. Fluids Eng.* 134 (10) (2012) 101304, <http://dx.doi.org/10.1115/1.4007335>.
- [12] M. Mortazavi, V. Le Chenadec, P. Moin, A. Mani, Direct numerical simulation of a turbulent hydraulic jump: turbulence statistics and air entrainment, *J. Fluid Mech.* 797 (2016) 60–94, <http://dx.doi.org/10.1017/jfm.2016.230>.
- [13] E. McKeogh, D. Ervine, Air entrainment rate and diffusion pattern of plunging liquid jets, *Chem. Eng. Sci.* 36 (7) (1981) 1161–1172, [http://dx.doi.org/10.1016/0009-2509\(81\)85064-6](http://dx.doi.org/10.1016/0009-2509(81)85064-6).
- [14] H. Chanson, R. Manasseh, Air entrainment processes in a circular plunging jet. Void fraction and acoustic measurements, *J. Fluids Eng., Trans. ASME* 125 (5) (2003) 910–921, <http://dx.doi.org/10.1115/1.1595672>.
- [15] X. Qu, L. Khezdar, D. Danciu, M. Labois, M. Lakehal, Characterization of plunging liquid jets: a combined experimental and numerical investigation, *Intl. J. Multiphase Flow* 37 (7) (2011) 722–731, <http://dx.doi.org/10.1016/j.ijmultiphaseflow.2011.02.006>.
- [16] K. Harby, S. Chiva, J. Muñoz-Cobo, An experimental study on bubble entrainment and flow characteristics of vertical plunging water jets, *Exp. Therm Fluid Sci.* 57 (2014) 207–220, <http://dx.doi.org/10.1016/j.expthermflusci.2014.04.004>.
- [17] M. Kramer, S. Wieprecht, K. Terheiden, Penetration depth of plunging liquid jets – a data driven modelling approach, *Exp. Therm Fluid Sci.* 76 (2016) 109–117, <http://dx.doi.org/10.1016/j.expthermflusci.2016.03.007>.
- [18] H. Wang, N. Slamet, G. Zhang, H. Chanson, Intrusive measurements of air-water flow properties in highly turbulent supported plunging jets and effects of inflow jet conditions, *Chem. Eng. Sci.* 177 (2018) 245–260, <http://dx.doi.org/10.1016/j.ces.2017.11.030>.
- [19] P. Cain, I. Wood, Instrumentation for aerated flow on a spillway, *J. Hydraul. Div. ASCE* 107 (HY11) (1981) 1407–1424.
- [20] H. Chanson, *Air Bubble Entrainment in Free-Surface Turbulent Shear Flows*, Academic Press, London, UK, 1997.
- [21] G. Zhang, H. Chanson, H. Wang, Total pressure fluctuations and two-phase flow turbulence in self-aerated stepped chute flows, *Flow Meas. Instrum.* 51 (2016) 8–20, <http://dx.doi.org/10.1016/j.flowmeasinst.2016.08.007>.
- [22] H. Chanson, S. Aoki, A. Hoque, Bubble entrainment and dispersion in plunging jet flows: freshwater versus seawater, *J. Coast. Res.* 22 (3) (2006) 664–677, <http://dx.doi.org/10.2112/03-0112.1>.
- [23] C. Gualtieri, H. Chanson, Effect of Froude number on bubble clustering in a hydraulic jump, *J. Hydraul. Res. IAHR* 48 (4) (2010) 504–508, <http://dx.doi.org/10.1080/00221686.2010.491688>.
- [24] H. Wang, Z. Hu, H. Chanson, Two-dimensional bubble clustering in hydraulic jumps, *Exp. Therm Fluid Sci.* 68 (2015) 711–721, <http://dx.doi.org/10.1016/j.expthermflusci.2015.07.006>.
- [25] H. Chanson, G. Carosi, Advanced post-processing and correlation analyses in high-velocity air–water flows, *Environ. Fluid Mech.* 7 (2007) 495–508, <http://dx.doi.org/10.1007/s10652-007-9038-3>.
- [26] E. McKeogh, *Study of Air Entrainment Using Plunging Water Jets*, PhD thesis Queen's University of Belfast, UK, 1978.
- [27] D. Ervine, E. McKeogh, E. Elsayy, Effect of turbulence intensity on the rate of air entrainment by plunging water jets, *Proc. Instn Civ. Engrs, UK (Part 2)* (1980) 425–445.
- [28] D. Chirichella, R. Gomez Ledesma, K. Kiger, J. Duncan, Incipient air entrainment in a translating axisymmetric plunging laminar jet, *Phys. Fluids* 14 (2002) 781–790.
- [29] N. Bertola, H. Wang, H. Chanson, Air bubble entrainment at vertical plunging jets: a large-scale experimental study, Hydraulic Model Report No. CH104/17, School of Civil Engineering, The University of Queensland, Brisbane, Australia, 2017.
- [30] H. Wang, S. Felder, H. Chanson, An experimental study of turbulent two-phase flow in hydraulic jumps and application of a triple decomposition technique, *Exp. Fluids* 55 (7) (2014) 1775, <http://dx.doi.org/10.1007/s00348-014-1775-8>.
- [31] D. Long, N. Rajaratnam, P. Steffler, P. Smy, Structure of flow in hydraulic jumps, *J. Hydraul. Res. IAHR* 29 (2) (1991) 207–218.
- [32] H. Wang, F. Murzyn, H. Chanson, Interaction between free-surface, two-phase flow and total pressure in hydraulic jump, *Exp. Therm Fluid Sci.* 64 (2015) 30–41, <http://dx.doi.org/10.1016/j.expthermflusci.2015.02.003>.
- [33] H. Chanson, Air entrainment in two-dimensional turbulent shear flows with partially developed inflow conditions, *Intl. J. Multiph. Flow* 21 (6) (1995) 1107–1121, [http://dx.doi.org/10.1016/0301-9322\(95\)00048-3](http://dx.doi.org/10.1016/0301-9322(95)00048-3).
- [34] H. Wang, F. Murzyn, Experimental assessment of characteristic turbulent scales in two-phase flow of hydraulic jump: from bottom to free surface, *Environ. Fluid Mech.* 17 (1) (2017) 7–25.